Hemodynamically efficient artificial right atrium design for univentricular heart patients

Heng Wei [*]
Department of Aerospace and Mechanical Engineering, University of Southern California, Los Angeles, California 90089, USA

Cynthia S. Herrington and John D. Cleveland
Division of Cardiac Surgery, Children's Hospital Los Angeles, Los Angeles, California 90027, USA

Vaughn A. Starnes
Division of Cardiac Surgery, Children's Hospital Los Angeles, Los Angeles, California 90027, USA and Division of Cardiac Surgery, Keck School of Medicine, University of Southern California, Los Angeles, California 90033, USA

Niema M. Pahlevan [†]
Department of Aerospace and Mechanical Engineering, University of Southern California, Los Angeles, California 90089, USA and Huntington Medical Research Institutes, Pasadena, California 91105, USA

(Received 16 July 2021; accepted 22 November 2021; published 16 December 2021)

Infants born with single-ventricle physiologies pose significant challenges for mechanical circulatory support devices. Their corresponding Fontan circulations consist of passive blood flow that returns to the lungs via direct connections to the pulmonary arteries without a pumping chamber. When Fontan patients reach adolescence or young adulthood, they tend to develop heart failure and may require heart transplants and/or mechanical assist devices. Mechanical supports often require a reservoir to attach, but no such blood reservoir exists in a closed Fontan circulation. This study was aimed to investigate the existence of a hemodynamically optimized geometry for an artificial right atrium (ARA) that can act as a reservoir for circulatory support in Fontan patients. Our hemodynamics-based criteria for an ARA were defined as minimum particle residence time (PRT) (to reduce the probability of blood clot formation) and maximum volume compliance (to prevent pressurization of cerebral and hepatic veins). A computational approach was used to complete this study. We utilized non-Newtonian fluid-solid interaction simulations constructed by lattice-Boltzmann and immersed boundary methods. Our results show that a hemodynamically optimum shape for an ARA with minimum PRT (relative to the cases considered in this study) is convex at the outlet (towards the lungs) and concave at the opposite side of the outlet. Additionally, the optimal ARA geometry well preserves the volume compliance that is needed to prevent pressurization of cerebral and/or hepatic veins. Interestingly, this shape resembles that of the healthy anatomical right atrium. Future implantation of our proposed ARA configuration may potentially lessen the risk of implementing biventricular supports in Fontan patients.

DOI: 10.1103/PhysRevFluids.6.123103

[*]weiheng@usc.edu
[†]pahlevan@usc.edu

I. INTRODUCTION AND BACKGROUND

Within the spectrum of surgical management for congenital heart diseases (CHD; occurrence varies between 4 and 50 patients per 1000 live births [1]), infants born with single-ventricle physiologies experience significant challenges throughout their lives [2]. Burdened with a univentricular heart (either a left or a right ventricle only), these patients are palliated through a series of three-staged surgical operations with the goal of improving systemic and pulmonary blood circulation. These operations are called Norwood [3], Glenn [4], and Fontan [5], which, together, are designed to dedicate the only ventricle to the systemic circulation (Norwood) and to recreate the pulmonary circulation through direct communication with the pulmonary arteries (Glenn and Fontan).

Due to recent advances in surgical techniques and patient care, more patients survive through all three stages [6] than in the past. However, since univentricular hearts are hemodynamically less efficient, these patients develop diastolic and/or systolic dysfunction. Eventually, they become heart transplant candidates as their level of heart failure progresses. Severe comorbidities occur in half of Fontan patients [7–9], and Fontan patients who survive the Fontan surgery have around a 20% mortality rate by the age of 20. Given the national shortage of available donor organs and correspondingly extended wait-list times, heart transplantation remains a limited treatment option (the number of donor hearts available for children is fixed at around 500 per year) [10]. Many institutions have attempted to support these patients with standard ventricular assist devices (VADs) until they can be given a transplant [11–14]. The primary difficulty in establishing mechanical support for Fontan concerns the lack of a blood reservoir for the pulmonary circulation in such diseased conditions. Several attempts have been made to recreate a tissue atrium but, unfortunately, they have uniformly failed [15,16].

In this paper, we theorized that an artificial right atrium (ARA), if appropriately designed and implanted in place of the Fontan graft, provides an adequate reservoir for blood that subsequently improves circulatory support. An ideal ARA should be clinically feasible; adjustable in volume (to account for changes in patient body surface area); compatible with all commercially available VADs; and possess efficient intracavitary flow (to prevent blood stagnation and clotting). Furthermore, it should decompress (depressurize) congested cerebral and hepatic veins. This decompression is clinically important since it can alleviate hepatic congestion, protein-losing enteropathy, and liver cirrhosis. Our goal in this study was to identify a hemodynamically optimized geometry for an artificial right atrium to be potentially employed for Fontan circulation. Our target hemodynamic characteristics were based on (1) minimizing particle residence time (PRT) and (2) preserving total volume compliance. In the present work, we treated blood as a non-Newtonian fluid (using the Carreau-Yasuda model) and employed a computational approach employing the lattice-Boltzmann method (LBM; for the fluid domain [17]) coupled with an immersed boundary method (IBM; for the solid domain [18]).

II. METHODOLOGY

A. Flow solver

1. The lattice Boltzmann method (LBM)

LBM uses simplified kinetic equations combined with a modified molecular-dynamics approach in order to simulate fluid flows. In essence, it is a methodology that is an alternative to the conventional continuum-based computational fluid dynamics (CFD) methods that use Navier-Stokes equations. The accuracy and usefulness of the LBM approach are well established for various fluid dynamics problems including turbulence [19], multiphase flow [20], and hemodynamics [21]. As highlighted in previous studies, LBM methods have been shown to be particularly valuable for simulating hemodynamics [19–22].

In such a method, the synchronous motions of the particles on a regular lattice are enforced through a particle distribution function. This distribution function enforces mass and momentum conservation. It also ensures that the fluid is Galilean invariant and isotropic [23]. In the present

work, a single-relaxation-time (SRT) incompressible lattice-Boltzmann method was used to solve the incompressible blood flow [24]. The evolution of the distribution functions on the lattice was governed by the discrete Boltzmann equation employing the BGK (Bhatnagar-Gross-Krook) collision model:

$$f_i(\boldsymbol{x}+\boldsymbol{e}_i\Delta t, t+\Delta t) - f_i(\boldsymbol{x}, t) = -\frac{1}{\tau}\left[f_i(\boldsymbol{x}, t) - f_i^{eq}(\boldsymbol{x}, t)\right] + \Delta t F_i, \tag{1}$$

where $f_i(\boldsymbol{x}, t)$ is the distribution function of the particles in phase space, $\boldsymbol{e}_i$ is the discrete velocity at position $\boldsymbol{x}$ and time t, τ is a nondimensional relaxation time, and f_i^{eq} is the equilibrium distribution function. Here, $i = 0, 1, \ldots, 18$ for a D3Q19 (19 discrete velocity vectors) stencil approach.

The nondimensional relaxation time, τ, is related to fluid viscosity μ as

$$\mu = \rho\nu = \rho c_s^2\left(\tau - \tfrac{1}{2}\right)\Delta t, \tag{2}$$

where ν is the kinematic viscosity; ρ is the incompressible fluid density (e.g. blood density); and $c_s = \frac{\Delta x}{\Delta t\sqrt{3}}$ is the lattice sound speed. The constants Δt and Δx are the time step and lattice space discretization size, respectively.

The equilibrium distribution function f_i^{eq} (for the incompressible lattice-Boltzmann model [24]) and the forcing term (F_i) [25] from Eq. (1) are defined respectively as

$$f_i^{eq} = \omega_i\rho_0 + \omega_i\rho\left[\frac{\boldsymbol{e}_i\cdot\boldsymbol{v}}{c_s^2} + \frac{(\boldsymbol{e}_i\cdot\boldsymbol{v})^2}{2c_s^4} - \frac{\boldsymbol{v}^2}{2c_s^2}\right], \tag{3}$$

$$F_i = \left(1 - \frac{1}{2\tau}\right)\omega_i\left(\frac{\boldsymbol{e}_i - \boldsymbol{v}}{c_s^2} + \frac{\boldsymbol{e}_i\cdot\boldsymbol{v}}{c_s^4}\boldsymbol{e}_i\right)\cdot\boldsymbol{f}, \tag{4}$$

where ω_i are weighting factors (equal to 1/3 for $i = 1$, to 1/18 for $i = 2$ to 7, and to 1/36 for the rest [24]). Note that, for our two-dimensional (2D) simulations, a D2Q9 stencil approach with nine discrete velocity sets is used instead. The lattice sound speed is the same as for 3D cases, and the corresponding weighting factors are equal to 4/9 for $i = 1$, to 1/9 for $i = 2, 3, 4, 5$, and to 1/36 for $i = 6, 7, 8, 9$.The variable ρ_o, related to the microscopic pressure ($\rho_o = \frac{p}{c_s^2}$) and the velocity $\boldsymbol{v}$ can be calculated respectively by the expressions

$$\rho_o = \sum_i f_i, \tag{5}$$

$$\rho\boldsymbol{v} = \sum_i \boldsymbol{e}_i f_i + \frac{1}{2}\boldsymbol{f}\Delta t. \tag{6}$$

2. *Fluid viscosity model*

The significance of non-Newtonian effects in Fontan circulation has been shown in previous studies [27,28]. In our simulations, blood was thusly modeled as a non-Newtonian fluid using the Carreau-Yasuda model, which has been widely used to account for the shear-thinning behavior of blood in hemodynamics simulations [22,26]. The model was curve fitted with Fontan patient-specific data provided by a prior study from Cheng *et al.* [26], as depicted in Fig. 1.

The apparent viscosity of the Carreau-Yasuda model is given by

$$\mu(\dot\gamma) = \mu_\infty + (\mu_o - \mu_\infty)[1 + (\lambda\dot\gamma)^a]^{\frac{n-1}{a}}, \tag{7}$$

where $\dot\gamma$ is the shear rate, μ_o is the zero shear viscosity, and μ_∞ is the Newtonian viscosity (when the shear rate goes to infinity). The constant parameters λ (the time constant), a, and n (the power-law index) are empirically determined. The main advantage of the model given by Eq. (7) is that it is continuous in $\dot\gamma \geqslant 0$. In the results that follow, values of $\mu_o = 56$ cP (1 cP = 0.001 Pa s), $\mu_\infty = 3.5$ cP, $\lambda = 3.133$ s, $a = 2$, and $n = 0.3568$ were employed as determined by patient-specific data from Cheng *et al.* [29].

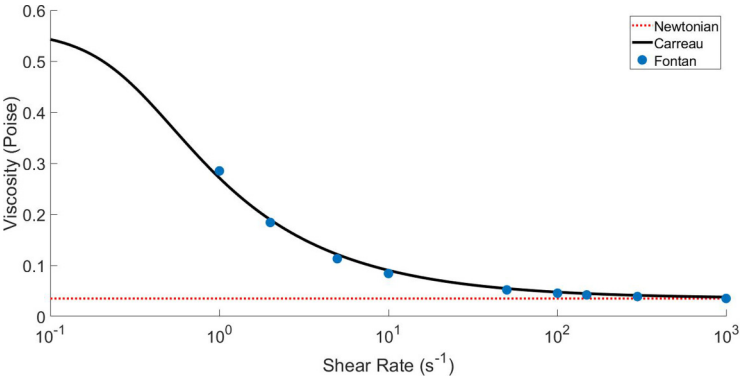

FIG. 1. The curve-fitted viscosities determined for the shear-thinning Carreau-Yasuda model using values provided by Fontan patient-specific data from Cheng *et al.* [26].

The shear-rate-dependent effect of non-Newtonian blood flow was implemented into the LBM using Eq. (7) together with Eq. (2) so that the microscopic relaxation time and the macroscopic fluid viscosity are fully coupled [22].

3. LBM *algorithm*

The core non-Newtonian LBM algorithm consists of a cyclic sequence of substeps, with each cycle corresponding to one time step:

1. Compute the macroscopic variables ρ_0 and $\boldsymbol{v}$ from f_i via Eqs. (5) and (6).
2. Obtain the equilibrium distribution f_i^{eq} from Eq. (3).
3. Compute the apparent viscosity μ at each point by Eq. (7) and calculate the local relaxation time τ from Eq. (2).
4. Perform collision (relaxation) and streaming (propagation) to update f_i via Eq. (1).

Further details concerning this particular LBM algorithm can be found in previous literature [22,24,30].

B. Solid solver

1. Compliant wall modeling

To describe in a Lagrangian coordinate system the deformation of the compliant wall of the artificial right atrium, the structure equation was considered as

$$\rho_s h \frac{\partial^2 \boldsymbol{X}}{\partial t^2} = \frac{\partial}{\partial s}\left[E_h\left(1-\left(\frac{\partial \boldsymbol{X}}{\partial s}\cdot\frac{\partial \boldsymbol{X}}{\partial s}\right)^{-1/2}\right)\frac{\partial \boldsymbol{X}}{\partial s} - \frac{\partial}{\partial s}\left(E_I\frac{\partial^2 \boldsymbol{X}}{\partial s^2}\right)\right] + \boldsymbol{F}_L, \tag{8}$$

where $\boldsymbol{X}(s,t)$ is the corresponding position of the solid wall in the Lagrangian coordinate, ρ_s is the density of the solid wall, h is the thickness of the wall, s is the Lagrangian coordinate parameterized along the solid wall, and $\boldsymbol{F}_L$ is the Lagrangian force exerted on the solid wall by the fluid. The constants E_h and E_I are the stretching and bending stiffnesses, respectively. The boundary conditions of the solid wall at a free head were defined as

$$1-\left(\frac{\partial \boldsymbol{X}}{\partial s}\cdot\frac{\partial \boldsymbol{X}}{\partial s}\right)^{-1/2} = 0, \quad \frac{\partial^2 \boldsymbol{X}}{\partial s^2} = (0,0), \quad \frac{\partial^3 \boldsymbol{X}}{\partial s^3} = (0,0), \tag{9}$$

and, at a fixed end, as

$$\boldsymbol{X} = \boldsymbol{X}_o, \quad \frac{\partial \boldsymbol{X}}{\partial s} = (-1,0). \tag{10}$$

The reference hydrodynamic quantities represented by fluid density ρ, velocity $U_\infty = Q/A$ [where A is the area of superior vena cava (SVC)], and length $L = D$ (where D is the diameter of SVC) are chosen to nondimensionalize the above expressions. The corresponding (nondimensional) parameters considered for the results that follow consist of the Reynolds number $\mathrm{Re} = \rho U_\infty L/\mu$, the bending coefficient $K = E_I/\rho U_\infty^2 L^3$, the tension coefficient $S = Eh/\rho U_\infty^2 L$, and the mass ratio of the solid wall to the fluid $M = \rho_s h/\rho L$. In this work, E_h is set to be equal to 5×10^2 Pa m with a wall thickness of $h = 1$ mm. The flexural rigidity of a shell (E_I) is 5×10^{-3} Pa m^3 (within physiological ranges [31–34]). The solid density is the same as the blood density, where the mass ratio M is equal to 0.05 for a thin wall (shell) model. Material properties were chosen to be within physiological range [35,36].

The solid deformation $\boldsymbol{X}(s,t)$, governed by Eq. (8), was solved using a nonlinear finite element method (FEM) solver as described by Doyle [37]. In such a solver, the large-displacement and small-strain deformation problem is handled by a corotational scheme [38], which uses three-node triangular elements to describe the deformation using six degrees of freedom (three displacement components and three angles of rotation) [39]. An iterative strategy was used for the time stepping of the corresponding nonlinear system of algebraic equations in order to ensure second-order accuracy. Further details on the finite-element method employed in this work can be found in [37]. In our study, triangular element meshes with more than 10 000 elements (about 5000 nodes) have been employed. The Δs of each element is set to be close to the Δx of the fluid mesh in order to ensure the stability of the fluid-solid coupling procedure.

2. Fluid-solid coupling

The immersed boundary method (IBM) [18] was used to couple the resulting fluid LBM and nonlinear solid FEM solvers [40,41]. IBM has been extensively used to simulate the fluid-solid interaction (FSI) problems in cardiovascular biomechanics [27,42–46]. The body force term f in Eq. (4) was considered as the interaction force between the fluid and the boundary in order to enforce the no-slip velocity condition at the FSI boundary. The Lagrangian force between the fluid and structure $\boldsymbol{F}_L$ was calculated using a penalty scheme [18] described by the expression

$$\boldsymbol{F}_L = \alpha \left[\int_0^t [\boldsymbol{V}_f(s,t') - \boldsymbol{V}_s(s,t')]dt' \right] + \beta[\boldsymbol{V}_f(s,t) - \boldsymbol{V}_s(s,t)],$$

where $\alpha = -10$ and $\beta = -1$ are negative penalty parameters whose values have been suggested by previous studies [41,47–49]. The material derivative $\boldsymbol{V}_s = \partial \boldsymbol{X}/\partial t$ is the velocity of a Lagrangian material point on the solid wall, and $\boldsymbol{V}_f$ is the fluid velocity at the position $\boldsymbol{X}$ given by

$$\boldsymbol{V}_f(s,t) = \int \boldsymbol{v}(\boldsymbol{x},t)\delta(\boldsymbol{x} - \boldsymbol{X}(s,t))d\boldsymbol{x}. \tag{11}$$

Here, $\boldsymbol{v}(\boldsymbol{x},t)$ is the fluid velocity in the fluid domain $\boldsymbol{x}$. The body force $\boldsymbol{f}$ on the Eulerian points can be calculated by the integral

$$\boldsymbol{f}(\boldsymbol{x},t) = -\int \boldsymbol{F}_L(s,t)\delta(\boldsymbol{x} - \boldsymbol{X}(s,t))ds, \tag{12}$$

where $\delta(\boldsymbol{x} - \boldsymbol{X}(s,t))$ is the Dirac delta function. In the results that follow, the body force f and the Lagrangian interaction force $\boldsymbol{F}_L$ were explicitly calculated using the penalty IBM strategy outlined above and then substituted into each of the fluid and solid Eqs. (4) and (8), respectively [18].

The overall numerical strategy employed in this study has been successfully applied to a wide range of FSI problems [41,47,48,50], including those concerning the dynamics of fluid flow over a circular flexible plate [41] and the dynamics of an inverted flexible plate [47]. A summary of the complete algorithm, including the FSI coupling procedure, is provided in Fig. 2.

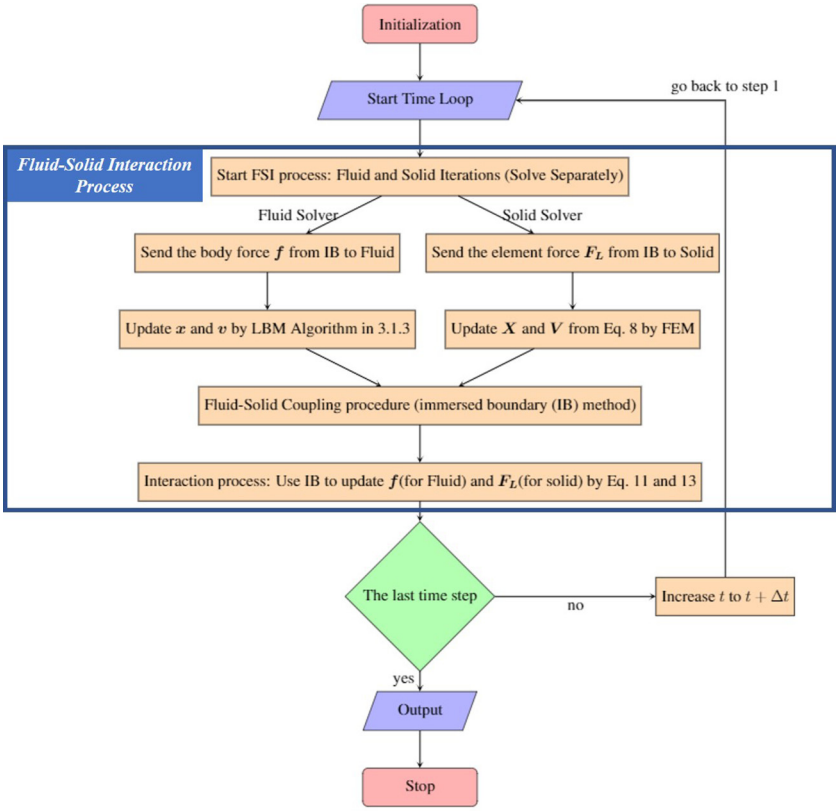

FIG. 2. A summary of the overall algorithm for the complete solver. FSI: fluid-solid interaction; IBM: immersed boundary method; LBM: Lattice-Boltzmann method; FEM: finite element method.

C. Hydraulic circuit configuration and dimensions for an artificial right atrium

The overall dimensions of the artificial right atrium (ARA) including inlet and outlet were selected to be within physiological range [7,26]. Specifically, we considered the diameters of the superior and inferior cava (SVC and IVC) to be $D_i = D = 1.2$ cm, and the diameter of the pulmonary artery outlet to be $D_o = 0.75D$ ($= 0.9$ cm) (Fig. 3).

D. Shape-selection procedure for hemodynamic optimization

The overall procedure for identifying a hemodynamically optimum shape for an ARA with minimum PRT (relative to the cases considered in this study) is summarized in Fig. 4. We assumed that the geometry of the long axis plane (LAP: the center plane with inlets and outlet; see Fig. 3) contributes the most to a particle's residence time. Therefore, our first step was to study the hemodynamics of flow in LAPs (of various shapes) using 2D models in which the cross-sectional area was preserved. We studied four relevant configurations of LAPs: sphere-like convex on both sides (LAP1); flat at the outlet but convex on the opposite side (LAP2); convex at the outlet and moderately concave on the opposite side (LAP3); and convex at the outlet and a concave curvature with a large radius (compared to LAP3) at the opposite side (LAP4). We additionally studied a T junction without stagnation as a reference for the minimum PRT. We did not consider cases where the outlet curvature is concave since the resulting outflow would be behind a stagnation point (and trivially produce the largest PRT). The schematics of all the considered 2D cases are

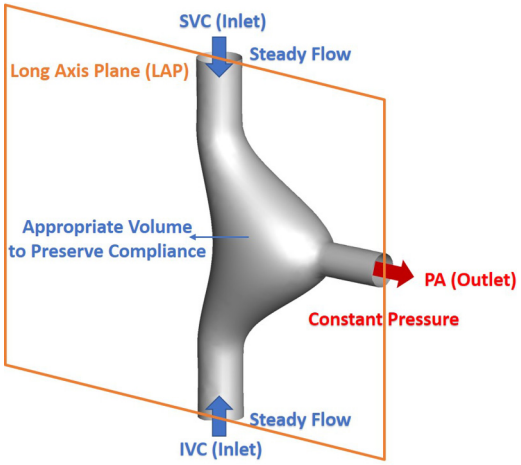

FIG. 3. Schematic of the artificial right atrium (ARA) circuit. The superior and inferior vena cava (SVC and IVC) are the inlets, and the pulmonary artery (PA) is the outlet. Bold arrows indicate the net direction of blood flow.

summarized and illustrated in Fig. 5. With such a 2D-LAP approach, we were able to identify the hemodynamically optimized LAP (LAP-opt) in which PRT was minimized.

Such 2D configurations were then extruded for 3D compliant FSI models of the ARA to further validate and study the significance of LAP geometry as well as to ensure that the geometry associated with LAP-opt does indeed yield a minimum PRT while preserving a high compliance value. The schematics of all the corresponding 3D compliant cases are summarized and illustrated in Fig. 6. Note that Case 1 and Case 2 are derived from the shapes of LAP1 and LAP2, respectively, whereas Case 3 and Case 4 employ the shape of LAP3 in their long-axis planes.

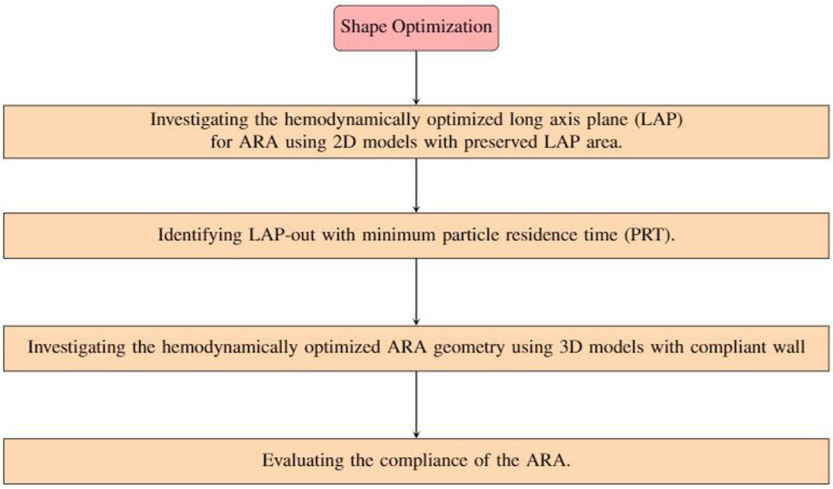

FIG. 4. Flow chart for the overall procedure of identifying hemodynamically optimum ARA shapes with minimum PRT (relative to the cases considered in this study). ARA: artificial right atrium; LAP: long-axis plane; PRT: particle residence time.

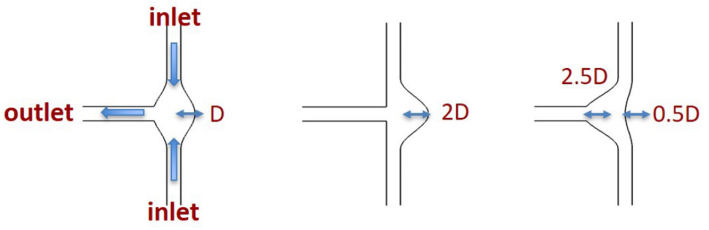

(a) LAP1 (b) LAP2 (c) LAP3

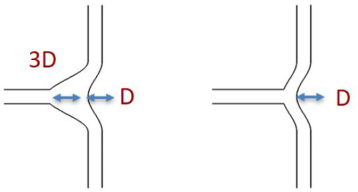

(d) LAP4 (e) Trivial T-junction

FIG. 5. Schematics of 2D LAP configurations investigated for identifying the LAP-opt. The SVC and IVC are the inlets, each with diameter $D_i = D = 1.2$ cm. The outlet represents the pulmonary artery circulation, with a diameter of $D_o = 0.75D$ ($= 0.9$) cm. The curvature for LAP1 is D at both the concave and convex sides; the curvature for LAP2 is $2.0D$ at the convex side; the curvature for LAP3 is $2.5D$ at the convex side and $0.5D$ at the concave side; and the curvature for LAP4 is $3.0D$ at the convex side and D at the concave side. Bold arrows indicate the net direction of the blood flow. LAP: log axis plane; SVC: superior vena cava; IVC: inferior vena cava.

E. Boundary conditions

An extension tube boundary model was used at inlets and outlets [51]. Specified steady flow rates of $Q = 1.5$ l/min with flat velocity profiles were applied at the inlet. With the extension tube boundary model, the flow becomes fully developed before entering the chamber (see the Appendix for the corresponding shape of the velocity profile at the inlet of the ARA). All simulations

(a) Case 1 (b) Case 2

(c) Case 3 (d) Case 4

FIG. 6. Schematics of the corresponding 3D compliant configurations. Cases 1, 2, and 3 have the same total volume. Case 4 is the reference case for the minimum particle residence time.

were continued until they reached steady state conditions. All results presented in this paper were collected when simulations (both for velocity and PRT) were fully converged to such steady states. Constant pressure ($p_0 = 10$ mmHg) was applied at the outlet. A no-slip condition was imposed at the fluid-solid interface. The compliant wall was considered as a linear elastic material with a Young's modulus of $E = 0.5$ MPa and a thickness of $h = 1$ mm. All the values are adopted based on the physiological range reported for young Fontan patients [7,26,31,32,36,36,52].

F. Numerical simulations

Simulations were performed in 2D for the five hemodynamic cases with different LAP shapes (to identify the optimum LAP) and in 3D for the four corresponding ARA configurations. We fixed the SVC/IVC flow proportion to be 50/50. A mesh size of $D/\Delta x = 40$ was used in all simulations. Mesh independence studies were performed to ensure the convergence of the calculations. In all cases, we employed a Reynolds number Re = 378 at the outlet and Re = 189 at each inlet, each determined by the expression

$$\mathrm{Re} = \frac{\rho U_{\mathrm{ref}} L_{\mathrm{ref}}}{\mu}, \tag{13}$$

where $U_{\mathrm{ref}} = Q/A$, $L_{\mathrm{ref}} = D$.

G. Hemodynamic analysis

Two clinically relevant fluid dynamics criteria were considered for the identification of the optimum ARA geometry with minimum PRT (relative to the cases considered in this study): (1) particle residence time (PRT) and (2) volume compliance. Minimum PRT is desirable since it reduces the chance of blood stagnation and clot formation, and maximum compliance is beneficial since it can prevent pressurization of hepatic and/or cerebral veins.

*1. Particle residence time (***PRT***)*

The PRT was determined by solving the partial differential equation given by

$$\frac{\partial \tau_p}{\partial t}\,|_x + \boldsymbol{u} \cdot \nabla \tau_p = H(\boldsymbol{x}), \quad \text{where } H(\boldsymbol{x}) = \begin{cases} 1 & \text{if } \boldsymbol{x} \in \Omega, \\ 0 & \text{otherwise.} \end{cases} \tag{14}$$

Here, τ_p is the total time that a particle occupies the subdomain Ω and $H(x)$ is the Heaviside function. The source term given by the Heaviside function ensures that time accumulates only when the particle is inside Ω. The corresponding spatial average $\mathrm{PRT}_{\mathrm{ave}}$ within a target area (e.g., inside an ARA) was determined by the expression [53]

$$\mathrm{PRT}_{\mathrm{ave}} = \frac{1}{\Omega} \int \tau_p(\boldsymbol{x}, \boldsymbol{t}) d\Omega. \tag{15}$$

In all the cases the particle residence time is nondimensionalized by $\|\boldsymbol{\tau_p}\|/T_{\mathrm{ref}}$, where $T_{\mathrm{ref}} = L_{\mathrm{ref}}/U_{\mathrm{ref}}$. In this study, Ω is defined as the complete physical domain of the artificial chamber (i.e., excluding the extension boundary model). Based on the definition above, the PRT quantifies how much time fluid particles have spent at a certain location after entering from the inlet. The value of the PRT is zero at the inlet since flow is downstream and the fluid particles at the inlet have just entered and could not have spent any time there. PRT is larger in stagnation regions since these particles have remained in the ARA chamber for a longer period of time since entering the ARA domain.

2. Volume compliance evaluation

We compared cases at the same total volume to ensure they all had similar base-level total volume compliance. Since geometry can affect the volume compliance of fluid flow, we evaluated

TABLE I. The averaged PRT determined from 2D simulations of LAP1–LAP4. LAP1–LAP4 have similar LAP areas. The T-junction configuration is the reference case for minimum PRT. PRT: particle residence time (PRT); LAP: long-axis plane.

Case	PRT_{ave}
LAP1	10.80
LAP2	11.50
LAP3	8.82
LAP4	8.90
T junction	7.56

the compliance for each chamber using the differentiation principle $C = \Delta V/\Delta P$, where we added a known volume (ΔV) of the blood into the chamber models and computed corresponding pressure changes (ΔP). The injected volume ΔV was chosen to be the same as the volume change in the steady flow simulation of the ARA (around 10% of the total ARA volume). This ensures that the computed compliance is close to the operating compliance of the ARA during flow simulations. The compliance values were compared against a spherical chamber with the same volume as the control case and whose compliance can be determined analytically as $C = \Delta V/\Delta P = 2\pi R^4/E_h$, where R is the radius of the sphere.

III. RESULTS

A. Hemodynamically optimized long-axis plane (LAP)

Table I presents the average particle residence time (PRT_{ave}) for each of the LAP cases (and T-junction reference case) as summarized by Fig. 5. The results of Fig. 7 illustrate PRT distributions for cases LAP1–LAP4. LAP3 demonstrates the lowest PRT whereas LAP2 demonstrates the highest (corresponding velocity distributions of each case are provided in the online supplementary materials).

B. 3D compliant artificial right atrium (ARA)

1. Averaged particle residence time (PRT_{ave})

Figure 8 presents the PRT distributions for the four cases of 3D compliant ARAs in their long-axis planes. Table II provides the corresponding values of PRT_{ave}, including those of the spherical control case. Percentage improvements from the sphere were defined relative to the baseline improvement of Case 4 (the model without an out-of-plane bulge, i.e., the lowest compliance) by

TABLE II. The averaged PRT determined from 3D simulations of the the 3D compliant ARA configurations. Note that Cases 1–3 have the same total volume. Percentage improvement is defined as $(PRT_{Sphere} - PRT)/(PRT_{Sphere} - PRT_{Case4}) \times 100$. PRT_{ave}: averaged particle residence time.

Case	PRT_{ave}	Percentage improvement
Sphere	14.81	0.00%
1	11.59	67.08%
2	12.18	54.79%
3	11.31	72.92%
4	10.01	100.00%

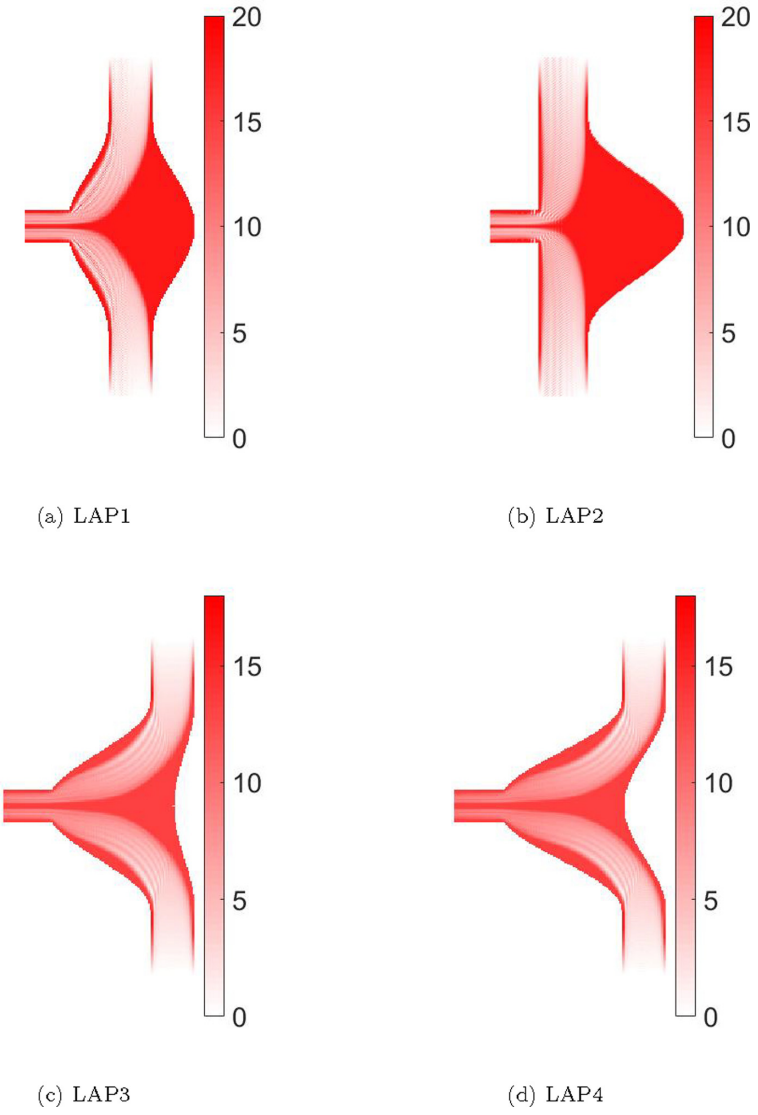

FIG. 7. PRT distributions determined by 2D simulations of LAP1–LAP4. All cases have similar LAP area.

the expression $(\mathrm{PRT}_{\mathrm{Sphere}} - \mathrm{PRT})/(\mathrm{PRT}_{\mathrm{Sphere}} - \mathrm{PRT}_{\mathrm{Case\ 4}}) \times 100$. Our results indicate that Case 3 (the model corresponding to LAP-opt) has the lowest PRT among ARAs with similar total volume, and that the sphere has (expectedly) the highest PRT.

2. Qualitative flow analysis

Figures 9 and 10 present velocity magnitudes (non-dimensionalized by $\|\boldsymbol{v}\|/U_{\mathrm{ref}}$) and streamlines for 3D compliant ARA models in their long-axis and short-axis planes, respectively. (Corresponding PRT distributions of the short-axis planes are provided in the Appendix.) The corresponding pressure distributions (nondimensionalized by $\boldsymbol{P}/\rho {U_{\mathrm{ref}}}^2$) in the long-axis plane are shown in Fig. 11. As expected, Case 4 has the highest overall pressure due to its low compliance volume.

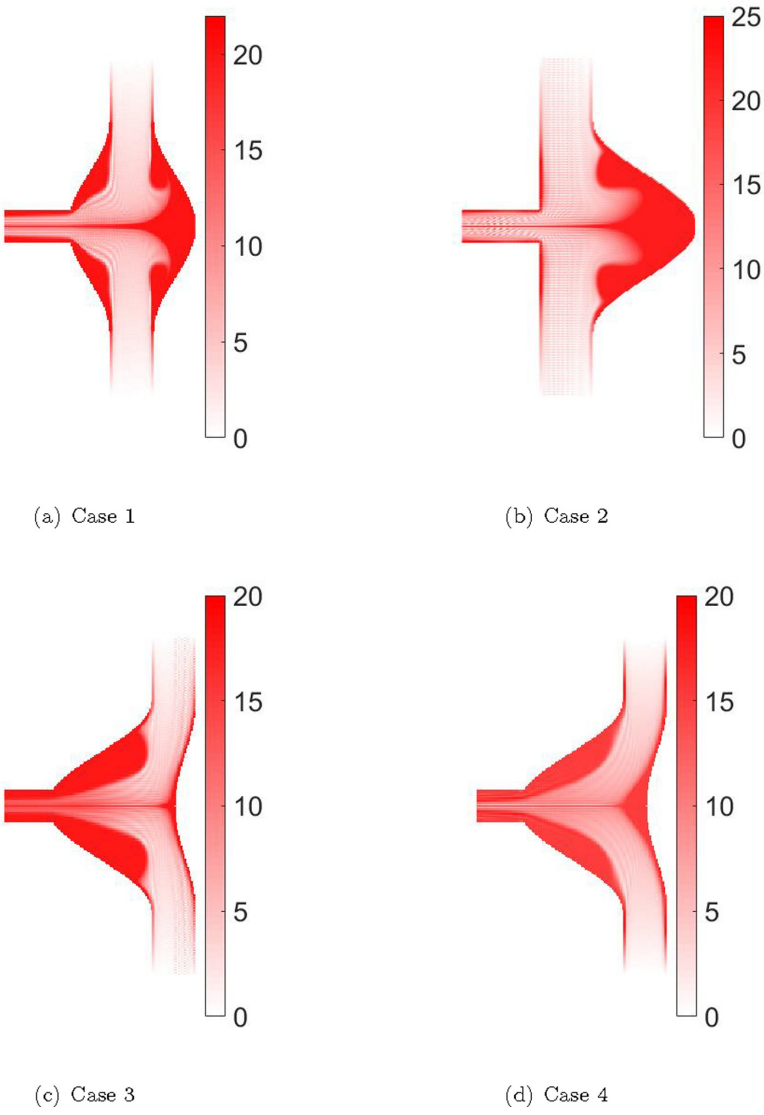

(a) Case 1 (b) Case 2

(c) Case 3 (d) Case 4

FIG. 8. PRT distributions in the long-axis plane determined by 3D FSI simulations of the compliant ARAs. Cases 1–3 have the same total volume. Case 4 has the same LAP as Case 3 but without the out-of-plane bulge (see Fig. 6).

3. Evaluation of the total volume compliance

Table III presents compliance values and net pressure rises for the 3D compliant ARA models. It also provides both analytically and numerically computed values corresponding to the trivial case of a sphere. The small differences observed for the sphere between analytical and numerical compliances is due to the added volume and fluid flow in the numerical model. The analytical solution is an ideal condition that assumes no flow motion exists. The numerical simulation is based on the added-volume method, which produces a small error in the compliance computation due to volume increase. As expected, Case 4 produces the lowest compliance (since it does not contain an out-of-plane bulge) and hence the highest pressure rise. Cases 1–3 have the same volume as the sphere. Case 3 has the highest compliance and lowest pressure drop among all ARA cases.

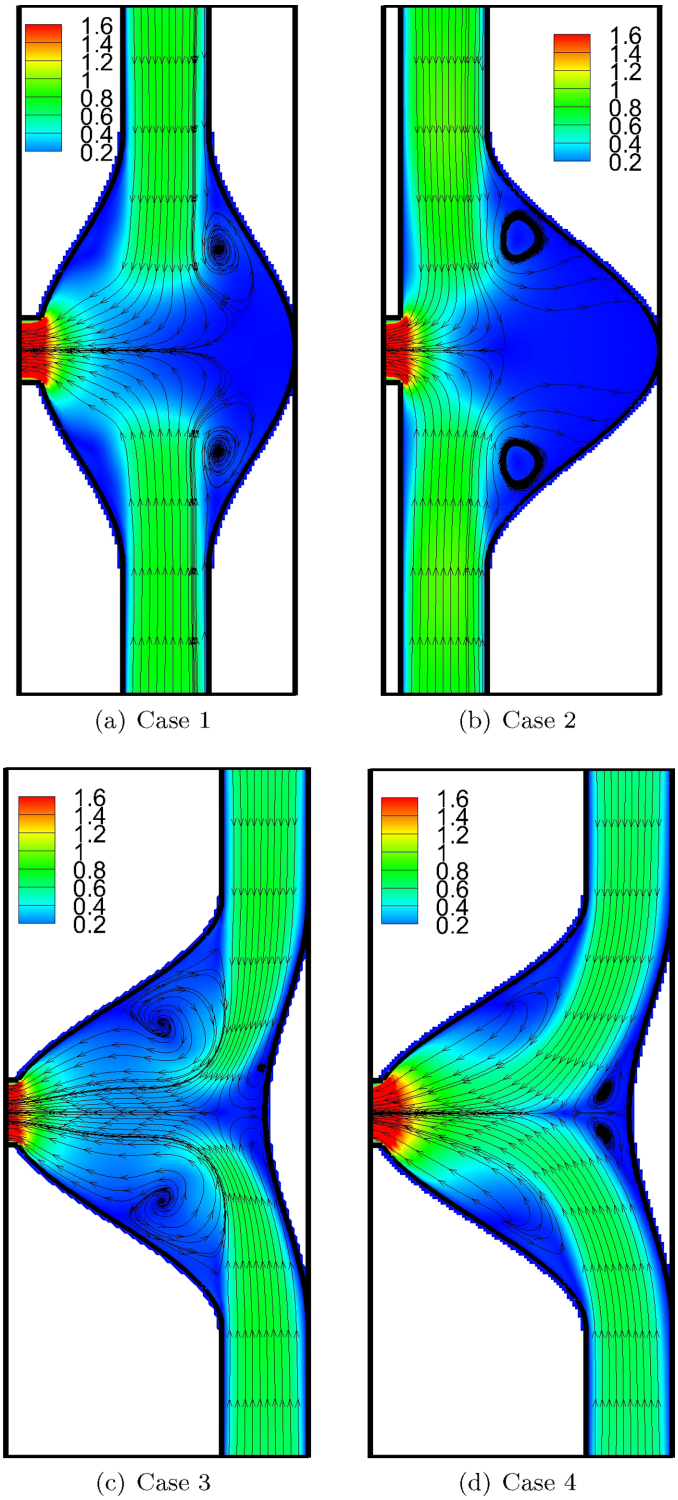

(a) Case 1 (b) Case 2

(c) Case 3 (d) Case 4

FIG. 9. Velocity magnitudes (nondimensionalized by $\|\boldsymbol{v}\|/U_{\text{ref}}$) and streamlines in the long-axis planes of the compliant ARA models. Cases 1–3 have the same overall volume. Case 4 has the same long-axis plane as Case 3, but it does not contain an out-of-plane bulge [hence lower volume compared to others, as shown in Fig. 6(d)].

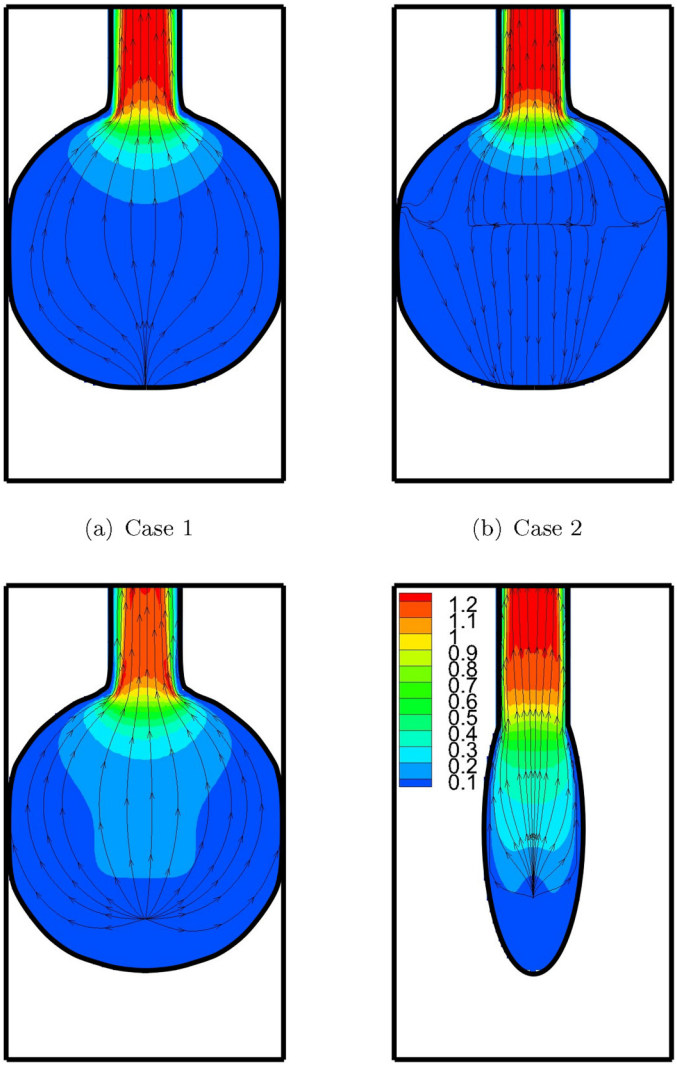

(a) Case 1 (b) Case 2

(c) Case 3 (d) Case 4

FIG. 10. Velocity magnitudes (nondimensionalized by $\|\boldsymbol{v}\|/U_{\text{ref}}$) and streamlines in short-axis planes of the compliant ARA models. Cases 1–3 have the same overall volume. Note that Case 4 contains the same long-axis plane as Case 3.

IV. DISCUSSION

In this study, we investigated the existence of a hemodynamically optimized geometry for an artificial right atrium (ARA) design. Our hemodynamics criteria consisted of the minimum particle residence time (PRT) and maximum volume compliance at a fixed total ARA volume. From a physiological point of view, low PRTs are important since they reduce the probability of blood clot formation. Volume compliance is also clinically important since low compliance can result in pressurization of cerebral and hepatic veins. The pressurization (compression) of the liver is of great clinical concern since it can promote hepatic congestion and liver cirrhosis.

We employed a computational approach where non-Newtonian (Carreau-Yasuda viscosity model-based) FSI simulations were produced by a lattice-Boltzmann method (LBM) coupled with

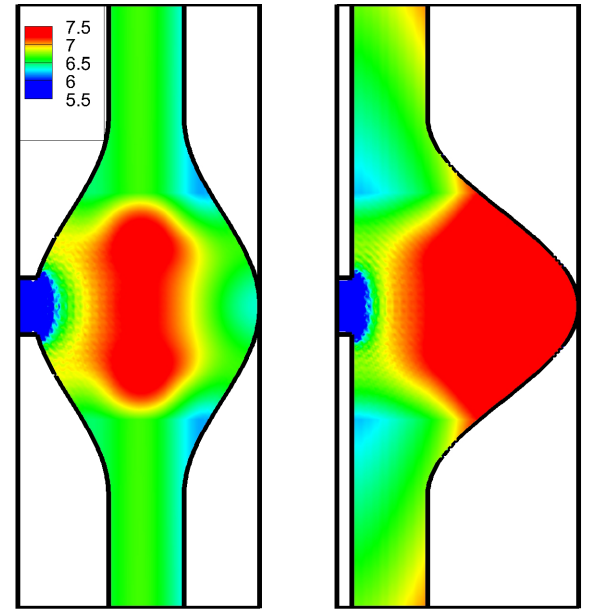

(a) Case 1 (b) Case 2

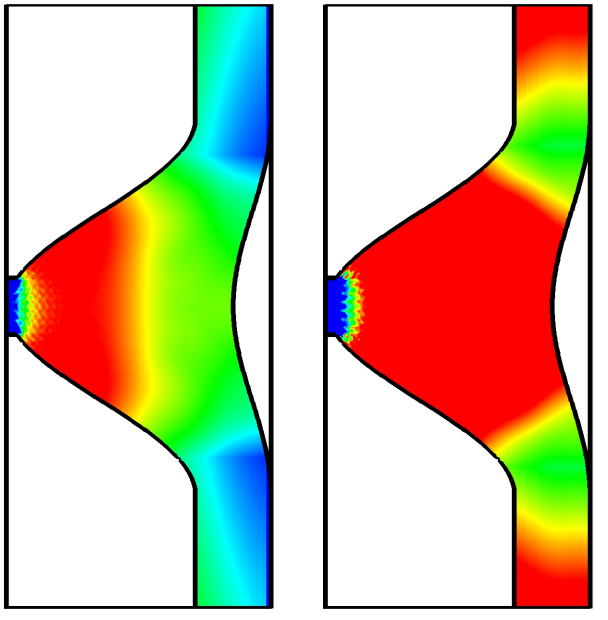

(c) Case 3 (d) Case 4

FIG. 11. Pressure distributions (nondimensionalized by $\boldsymbol{P}/\rho {U_{\mathrm{ref}}}^2$) in long-axis planes of compliant 3D ARA models. As expected, Case 4 has the highest overall pressure due to its low volume compliance.

an immersed boundary method (IBM). We first studied the shape of the long-axis plane (LAP) in an ARA by using 2D models to identify the optimum cross-sectional shape of an ARA in which PRT is minimized (LAP-opt, i.e., LAP3). We then extruded these LAP shapes to 3D compliance models of ARAs in order to confirm that the ARAs with LAP-opt Cases 3 and 4 have the lowest

TABLE III. Calculated values of compliance C ($m^3/Pa \times 10^{-10}$) and pressure rise P for the 3D compliant models. Cases 1–3 have the same volume as the sphere. The percent reduction in C is determined as $(C_{\text{Sphere (Analytical)}} - C)/C_{\text{Sphere (Analytical)}}$. The percent difference in P is determined as $(P - P_{\text{Sphere (Numerical)}})/P_{\text{Sphere (Numerical)}}$.

Case	C	% C Reduction	P (SVC/IVC) ($P/\rho U^2$)	% P difference
Sphere (Analytical)	5.6537	0.00%	N/A	N/A
Sphere (Numerical)	5.5779	1.34%	5.55	0.00%
1	4.6274	18.15%	6.67	20.18%
2	4.3176	23.63%	6.98	25.77%
3	4.8447	14.31%	6.45	16.22%
4	3.7119	34.35%	7.55	36.04%

PRT when the total volume is preserved. Our results ultimately suggest that a configuration with a concave curvature at the outlet and a convex curvature at the inlet is associated with minimized PRT (as demonstrated in Table I). This can be attributed to a reduction in the concentration of particles behind the stagnation point (see Fig. 7). Although this configuration comes with the expense of a slight increase in PRT at the outlet, it still provides the minimum PRT among all other relevant LAP configurations. Additionally, our results demonstrate that an LAP with moderately concave curvature (moderate radius) ($0.5D$) on the opposite side produces the minimum PRT in the long-axis plane (i.e., LAP-opt = LAP3).

The results summarized in Table II suggest that Cases 3 and 4 (ARAs corresponding to LAP-opt) do indeed produce the smallest PRT_{ave} over the entire ARA volume, even though the visualizations of Fig. 9 and 10 indicate in these cases that the concave shapes on the opposite sides create large vortices near the outlet. These vortices and the stagnation areas are the main causes of PRT increase (Fig. 8). However, they occupy significantly less space than those associated with the nonconcave Cases 1 and 2. Overall, two flow regimes with high PRT exist in each ARA: (1) the stagnation area and vortices close to the outlet, and (2) the stagnation region and vortices at the opposite side of the outlet. Based on our results, the contribution of outlet stagnation regions and vortices on the elevated PRT values is significantly less than those of the opposite side of the outlet. This is mainly due to the fact that particles trapped around the outlet have a higher chance of exiting the ARA domain than the fluid particles trapped on the opposite side of the outlet. It can be observed in Fig. 9 that the primary exit pathway for the opposite-side particles (those trapped in stagnation regions or vortices of the opposite side of the outlet) is through the narrow centerline "strip." This is the main reason that PRT is observed to be large around the centerline. In other words, the PRT is high in the narrow centerline stripe since it is occupied by "old" particles that have been trapped on the opposite side for a long time. This means that when the stagnation area and vortices are not close to the outlet, blood clotting is more likely to occur. Therefore, in order to obtain an ARA shape with minimized PRTs, the stagnation region at the opposite side of the outlet should be minimized (similarly to Case 3). Comparing the corresponding pressure distributions between Cases 3 and 4 (corresponding to minimal PRTs) in Fig. 11 demonstrates that Case 3 carries the lowest pressure compared to all the other cases. This suggests that Case 3 (which contains an out-of-plane bulge) could be a suitable configuration for preventing overpressurization of the IVC (liver) and SVC (brain), in contrast to the large SVC/IVC pressures observed in Case 4 (due to its low total volume compliance resulting from lack of such a bulge). Further analysis of the differences in pressure rises produced by various LAP geometries (Table III) additionally demonstrates that Case 3 provides the largest compliance with the lowest resultant pressure (although the reference spherical case provides better ratios, it is not hemodynamically efficient since it has the highest PRTs).

Overall, both qualitative and quantitative comparisons suggest that LAP3, with a convex curvature at the outlet and a concave curvature at the inlet, produces the minimum PRT (LAP-opt), and

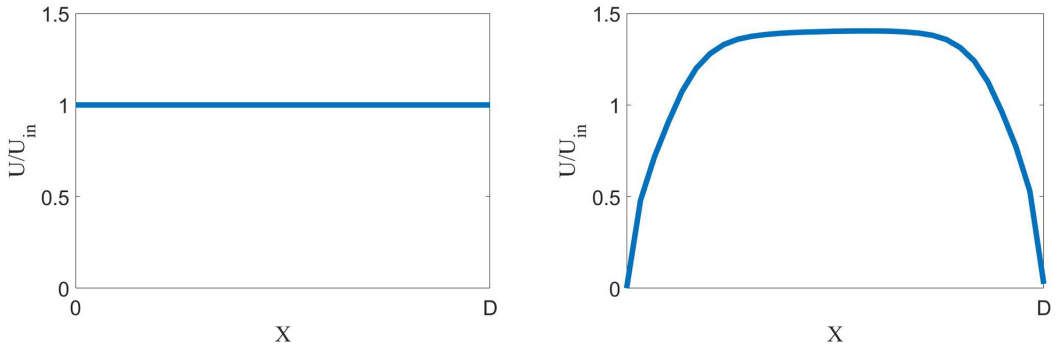

FIG. 12. Uniform flat velocity profile at the inlet of the extension tube boundary model (left) and the corresponding fully developed velocity profile at the entrance of the ARA (right).

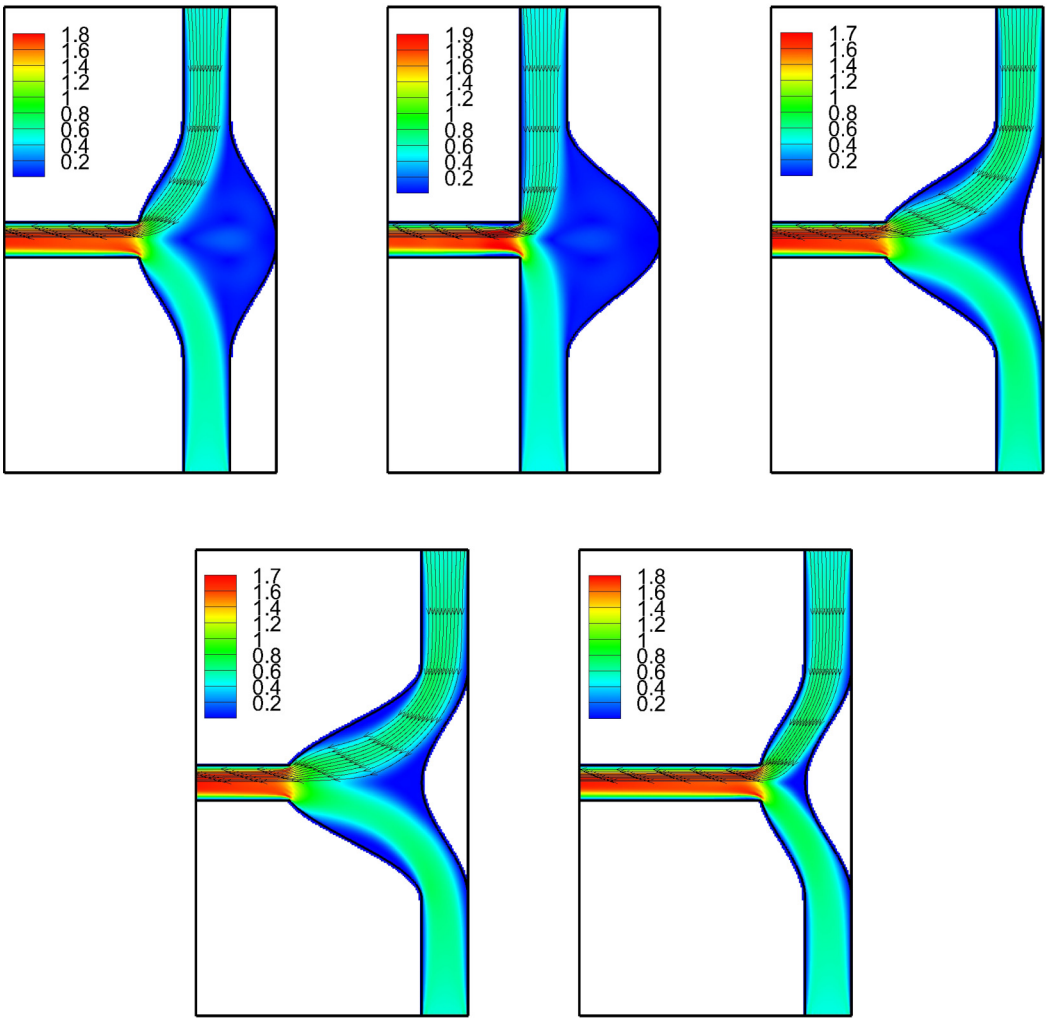

FIG. 13. Velocity magnitudes (nondimensionalized by $\|\boldsymbol{v}\|/U_{\text{ref}}$) for the 2D LAP cases.

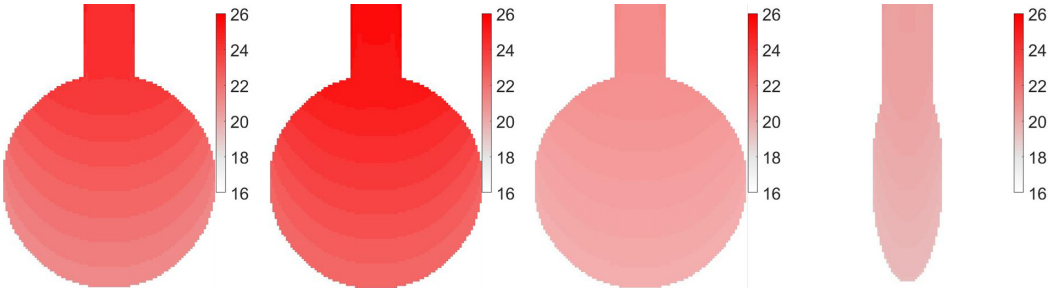

FIG. 14. PRT on short-axis planes at centerline (Cases 1 to 4 from left to right).

that the 3D compliant ARA associated with LAP3 that contains a bulge (Case 3) is the preferable design configuration with the highest volume compliance. Interestingly, the most hemodynamically efficient design suggested by our results is similar in shape to a healthy anatomical right atrium.

A. Limitations

One notable limitation of this study is that only steady flow was considered. There is no right ventricle in the Fontan circulation. In the absence of the hydraulic pulsatile force of the right ventricle, Fontan circulation is a single "pump" circulatory system with passive, nonpulsatile flow to the lungs (pulmonary arteries) [54]. Thus, we only consider steady cases since there is no flow pulsatility except for a negligible pressure pulsation crosstalk that might exist in some patients between arterial vessels (i.e., aorta and carotids) and large veins (i.e., SVC, IVC, jugular vein). However, small amplitude flow pulsations may propagate back into the ARA if a pulsatile-type assist device is connected to the ARA [52,55]. The effect of the corresponding pulsatile flow on the performance of our proposed ARA is beyond the scope of this paper and is a subject of future studies. Although pulsatile flow may not affect the overall findings of this study (i.e., the best shape for minimization of particle residence time and preservation of compliance), it may induce different dynamic behaviors including collapse and self-excitation. Future experimental studies are needed to confirm that our proposed optimal ARA geometry is not suboptimal when it comes to self-excitation and collapse. We also did not consider the complete material mechanics of the wall (e.g., viscoelasticity, isotropy, and nonlinearity). Future studies are needed to identify what type of material is best suited for an artificial right atrium.

B. Clinical implications

The series of operations used to palliate infants with single-ventricle diseases have improved outcomes over the last thirty years. Instead of dying in infancy, they now survive until adolescence or young adulthood, although eventually dying of heart failure with a failing Fontan circulation. Single-ventricle cardiac diseases encompass hypoplastic left heart syndrome, severe Shone's syndrome, hypoplastic right heart syndrome, and severely unbalanced AV canal defects. The sequence of procedures for repair of all these lesions ends with the Fontan. Ultimately, patients may become cardiac transplant candidates. Unfortunately, the use of mechanical support for these patients (while they sit on such transplant waiting lists) has proved to be difficult [13,15,16]. The major issue is that Fontan patients lack a right-sided compliance that can be attached to ventricular-assist devices. In circumstances where both right and left heart support is needed, there is no standardized way to successfully perform such support, particularly for the right heart. By removing the Fontan graft and replacing it with a hemodynamically optimized ARA, the required reservoir can hopefully be provided.

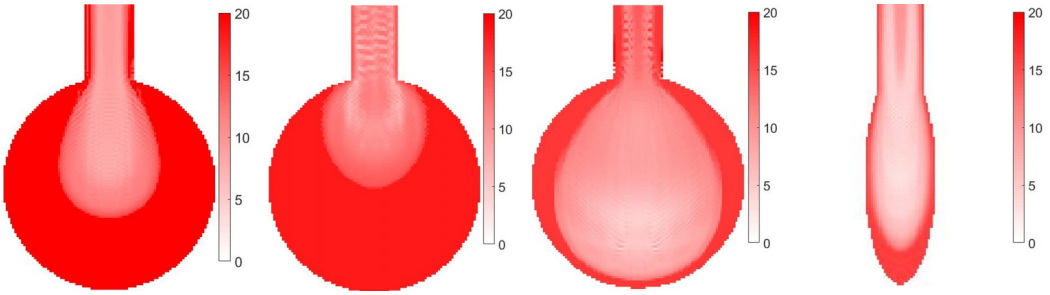

FIG. 15. PRT on short-axis planes at slightly higher ($0.2D$) than the centerline (Cases 1 to 4 from left to right).

C. Conclusions

In this study, we proposed a hemodynamically optimized geometry for an artificial right atrium (ARA) suitable for Fontan circulation. The implantation of the ARA can potentially lessen the risk of biventricular support in Fontan patients. Such an ARA can also be connected to currently available FDA-approved ventricular assist devices. Our results indicate that the overall optimum shape of an ARA with minimum PRT (relative to the cases considered in this study) is convex at the outlet (towards the lungs) and concave at the opposite side of the outlet, which not coincidentally also resembles the actual healthy human right atrium [56–58]. The proposed ARA geometry can also reduce the risk of thrombosis and blood clotting (via the minimization of the PRT) and also prevent the pressurization of cerebral and/or hepatic veins in Fontan circulation (via the preservation of volume compliance).

ACKNOWLEDGMENTS

The authors wish to acknowledge the financial support for this work provided by grants from Children's Hospital Los Angeles and the University of Southern California.

APPENDIX

See Figs. 12–15 for velocity magnitudes for the 2D LAP cases and PRT on short-axis planes.

[1] J. I. Hoffman and S. Kaplan, The incidence of congenital heart disease, J. Am. Coll. Cardiol. **39**, 1890 (2002).

[2] E. R. Griffiths, A. K. Kaza, M. C. W. von Ballmoos, H. Loyola, A. M. Valente, E. D. Blume, and P. del Nido, Evaluating failing Fontans for heart transplantation: predictors of death, Ann. Thorac. Surg. **88**, 558 (2009).

[3] W. I. Norwood, Jr., Hypoplastic left heart syndrome, Ann. Thorac. Surg. **52**, 688 (1991).

[4] G. J. Bittle, D. Morales, N. Pietris, N. Parchment, D. Parsell, K. Peck, K. B. Deatrick, L. Rodriguez-Borlado, R. R. Smith, L. Marbán, and S. Kaushal, Exosomes isolated from human cardiosphere-derived cells attenuate pressure overload-induced right ventricular dysfunction, J. Thorac. Cardiovasc. Surg. **162**, 975 (2021).

[5] W. I. Norwood Jr., M. L. Jacobs, and J. D. Murphy, Fontan procedure for hypoplastic left heart syndrome, Ann. Thorac. Surg. **54**, 1025 (1992).

[6] A. D. McCormick and K. R. Schumacher, Transplantation of the failing Fontan, Transl. Pediatr. **8**, 290 (2019).

[7] A. L. Cheng, C. P. Wee, N. M. Pahlevan, and J. C. Wood, A 4D flow MRI evaluation of the impact of shear-dependent fluid viscosity on in vitro Fontan circulation flow, Am. J. Physiol.: Heart Circ. Physiol. **317**, H1243 (2019).

[8] C. Poh and Y. d'Udekem, Life after surviving Fontan surgery: A meta-analysis of the incidence and predictors of late death, Heart Lung Circ. **27**, 552 (2018).

[9] C. Schilling, K. Dalziel, R. Nunn, K. Du Plessis, W. Y. Shi, D. Celermajer, D. Winlaw, R. G. Weintraub, L. E. Grigg, D. J. Radford *et al.*, The Fontan epidemic: Population projections from the Australia and New Zealand Fontan registry, Int. J. Cardiol. **219**, 14 (2016).

[10] D. Lloyd-Jones, R. Adams, T. Brown, M. Carnethon, S. Dai, G. De Simone, T. Ferguson, E. Ford, K. Furie, C. Gillespie *et al.*, Executive summary: Heart disease and stroke statistics—2010 update: A report from the American Heart Association, Circulation **121**, 948 (2010).

[11] J. B Clark, L. B Pauliks, J. L Myers, and A. Undar, Mechanical circulatory support for end-stage heart failure in repaired and palliated congenital heart disease, Curr. Cardiol. Rev. **7**, 102 (2011).

[12] L. W. Miller, Left ventricular assist devices are underutilized, Circulation **123**, 1552 (2011).

[13] M. Griselli, R. Sinha, S. Jang, G. Perri, and I. Adachi, Mechanical circulatory support for single ventricle failure, Front. Cardiovasc. Med. **5**, 115 (2018).

[14] A. L. Marsden, Y. Bazilevs, C. C. Long, and M. Behr, Recent advances in computational methodology for simulation of mechanical circulatory assist devices, Wiley Interdiscip. Rev.: Syst. Biol. Med. **6**, 169 (2014).

[15] C. L. Poh, R. Chiletti, D. Zannino, C. Brizard, I. E. Konstantinov, S. Horton, J. Millar, and Y. d'Udekem, Ventricular assist device support in patients with single ventricles: The Melbourne experience, Interact. Cardiovasc. Thorac. Surg. **25**, 310 (2017).

[16] J. R. Miller, T. S. Lancaster, C. Callahan, A. M. Abarbanell, and P. Eghtesady, An overview of mechanical circulatory support in single-ventricle patients, Transl. Pediatr. **7**, 151 (2018).

[17] M. Ashrafizaadeh and H. Bakhshaei, A comparison of non-Newtonian models for lattice Boltzmann blood flow simulations, Comput. Math. Appl. **58**, 1045 (2009).

[18] D. Goldstein, R. Handler, and L. Sirovich, Modeling a no-slip flow boundary with an external force field, J. Comput. Phys. **105**, 354 (1993).

[19] J. Cosgrove, J. Buick, S. Tonge, C. Munro, C. Greated, and D. Campbell, Application of the lattice Boltzmann method to transition in oscillatory channel flow, J. Phys. A: Math. Gen. **36**, 2609 (2003).

[20] X. Shan and H. Chen, Lattice Boltzmann model for simulating flows with multiple phases and components, Phys. Rev. E **47**, 1815 (1993).

[21] H. Fang, Z. Wang, Z. Lin, and M. Liu, Lattice Boltzmann method for simulating the viscous flow in large distensible blood vessels, Phys. Rev. E **65**, 051925 (2002).

[22] J. Boyd, J. M. Buick, and S. Green, Analysis of the Casson and Carreau-Yasuda non-Newtonian blood models in steady and oscillatory flows using the lattice Boltzmann method, Phys. Fluids **19**, 093103 (2007).

[23] D. A. Wolf-Gladrow, *Lattice-Gas Cellular Automata and Lattice Boltzmann Models: An Introduction* (Springer, Berlin, 2004).

[24] X. He and L.-S. Luo, Lattice Boltzmann model for the incompressible Navier-Sstokes equation, J. Stat. Phys. **88**, 927 (1997).

[25] X. He, X. Shan, and G. D. Doolen, Discrete Boltzmann equation model for nonideal gases, Phys. Rev. E **57**, R13 (1998).

[26] A. L. Cheng, N. M. Pahlevan, D. G. Rinderknecht, J. C. Wood, and M. Gharib, Experimental investigation of the effect of non-Newtonian behavior of blood flow in the Fontan circulation, Eur. J. Mech. B Fluids **68**, 184 (2018).

[27] H. Wei, A. L. Cheng, and N. M. Pahlevan, On the significance of blood flow shear-rate-dependency in modeling of Fontan hemodynamics, Eur. J. Mech.-B/Fluids **84**, 1 (2020).

[28] Z. Wei, S. Singh-Gryzbon, P. M. Trusty, C. Huddleston, Y. Zhang, M. A. Fogel, A. Veneziani, and A. P. Yoganathan, Non-Newtonian effects on patient-specific modeling of Fontan hemodynamics, Ann. Biomed. Eng. **48**, 2204 (2020).

[29] B. M. Johnston, P. R. Johnston, S. Corney, and D. Kilpatrick, Non-Newtonian blood flow in human right coronary arteries: Steady state simulations, J. Biomech. **37**, 709 (2004).
[30] K. Timm, H. Kusumaatmaja, and A. Kuzmin, *The Lattice Boltzmann Method: Principles and Practice* (Springer, Cham, 2016).
[31] N. M. Pahlevan and M. Gharib, A bio-inspired approach for the reduction of left ventricular workload, PLoS ONE **9**, e87122 (2014).
[32] N. M. Pahlevan and M. Gharib, Aortic wave dynamics and its influence on left ventricular workload, PLoS ONE **6**, e23106 (2011).
[33] N. M. Pahlevan and S. P. Mazandarani, Estimation of wave condition number from pressure waveform alone and its changes with advancing age in healthy women and men, Front. Physiol. **11**, 313 (2020).
[34] M. Gharib and M. Beizaie, Correlation between negative near-wall shear stress in human aorta and various stages of congestive heart failure, Ann. Biomed. Eng. **31**, 678 (2003).
[35] Y.-C. Fung, *Biomechanics: Mechanical Properties of Living Tissues* (Springer, New York, 2013).
[36] C. Vlachopoulos, M. O'Rourke, and W. W. Nichols, *McDonald's Blood Flow in Arteries: Theoretical, Experimental and Clinical Principles* (CRC, Boca Raton, FL, 2011).
[37] J. F. Doyle, *Nonlinear Analysis of Thin-Walled Structures: Statics, Dynamics, and Stability* (Springer, New York, 2013).
[38] H. Dai, H. Luo, and J. F. Doyle, Dynamic pitching of an elastic rectangular wing in hovering motion, J. Fluid Mech. **693**, 473 (2012).
[39] J.-L. Batoz, K.-J. Bathe, and L.-W. Ho, A study of three-node triangular plate bending elements, Int. J. Numer. Methods Eng. **15**, 1771 (1980).
[40] W.-X. Huang, S. J. Shin, and H. J. Sung, Simulation of flexible filaments in a uniform flow by the immersed boundary method, J. Comput. Phys. **226**, 2206 (2007).
[41] R.-N. Hua, L. Zhu, and X.-Y. Lu, Dynamics of fluid flow over a circular flexible plate, J. Fluid Mech. **759**, 56 (2014).
[42] C. S. Peskin, The immersed boundary method, Acta Numer. **11**, 479 (2002).
[43] R. Mittal and G. Iaccarino, Immersed boundary methods, Annu. Rev. Fluid Mech. **37**, 239 (2005).
[44] W.-B. Tay, Y.-H. Tseng, L.-Y. Lin, and W.-Y. Tseng, Towards patient-specific cardiovascular modeling system using the immersed boundary technique, Biomed. Eng. Online **10**, 1 (2011).
[45] B. Griffith, D. McQueen, and C. Peskin, Simulating cardiovascular fluid dynamics by the immersed boundary method, in *47th AIAA Aerospace Sciences Meeting including The New Horizons Forum and Aerospace Exposition* (AIAA, Reston, VA, 2009), p. 158.
[46] A. Yakhot, L. Grinberg, and N. Nikitin, Modeling rough stenoses by an immersed-boundary method, J. Biomech. **38**, 1115 (2005).
[47] C. Tang, N.-S. Liu, and X.-Y. Lu, Dynamics of an inverted flexible plate in a uniform flow, Phys. Fluids **27**, 073601 (2015).
[48] H. Ye, H. Wei, H. Huang, and X.-y. Lu, Two tandem flexible loops in a viscous flow, Phys. Fluids **29**, 021902 (2017).
[49] C. Zhang, H. Huang, and X.-Y. Lu, Free locomotion of a flexible plate near the ground, Phys. Fluids **29**, 041903 (2017).
[50] H. Huang, H. Wei, and X.-Y. Lu, Coupling performance of tandem flexible inverted flags in a uniform flow, J. Fluid Mech. **837**, 461 (2018).
[51] N. M. Pahlevan, F. Amlani, M. H. Gorji, F. Hussain, and M. Gharib, A physiologically relevant, simple outflow boundary model for truncated vasculature, Ann. Biomed. Eng. **39**, 1470 (2011).
[52] P. M. Trusty, M. Tree, K. Maher, T. C. Slesnick, K. R. Kanter, A. P. Yoganathan, and S. R. Deshpande, An in vitro analysis of the PediMag and CentriMag for right-sided failing Fontan support, J. Thorac. Cardiovasc. Surg. **158**, 1413 (2019).
[53] C. Long, M. Esmaily-Moghadam, A. Marsden, and Y. Bazilevs, Computation of residence time in the simulation of pulsatile ventricular assist devices, Comput. Mech. **54**, 911 (2014).
[54] T. B. Fredenburg, T. R. Johnson, and M. D. Cohen, The Fontan procedure: Anatomy, complications, and manifestations of failure, Radiographics **31**, 453 (2011).

[55] P. M. Trusty, M. Tree, D. Vincent, J. P. Naber, K. Maher, A. P. Yoganathan, and S. R. Deshpande, In vitro examination of the VentriFlo true pulse pump for failing Fontan support, Artif. Organs **43**, 181 (2019).
[56] F. F. Faletra, S. Y. Ho, and A. Auricchio, Anatomy of right atrial structures by real-time 3D transesophageal echocardiography, JACC: Cardiovasc.r Imaging **3**, 966 (2010).
[57] R. Shereen, S. Lee, S. Salandy, W. Roberts, and M. Loukas, A comprehensive review of the anatomical variations in the right atrium and their clinical significance, Transl. Res. Anat. **17**, 100046 (2019).
[58] M. Tadic, The right atrium, a forgotten cardiac chamber: An updated review of multimodality imaging, J. Clin. Ultrasound **43**, 335 (2015).